Fast and accurate flow measurement through dual-camera light field particle image velocimetry and ordered-subset algorithm

Xiaoyu Zhu (朱效宇),[1] Chuanlong Xu (许传龙),[1,a)] Md. Moinul Hossain,[2] Boo Cheong Khoo[3]

[1] National Engineering Research Center of Power Generation Control and Safety, School of Energy and Environment, Southeast University, Nanjing 210096, China

[2] School of Engineering, University of Kent, Canterbury, Kent, CT2 7NT, UK

[3] Department of Mechanical Engineering, National University of Singapore, 119260, Singapore

[a)]Authors to whom correspondence should be addressed: *chuanlongxu@seu.edu.cn*

Abstract: Light field particle image velocimetry (LF-PIV) can measure the three-dimensional (3D) flow field via a single perspective and hence is very attractive for applications with limited optical access. However, the flow velocity measurement via single camera LF-PIV shows poor accuracy in the depth direction due to the particle reconstruction elongation effect. This study proposes a solution based on a dual-camera LF-PIV system along with an ordered-subset simultaneous algebraic reconstruction technique (OS-SART). The proposed system improves the spatial resolution in the depth direction and reduces the reconstruction elongation. The OS-SART also reduces the computational time brought by the dual-camera LF-PIV. Numerical reconstructions of the particle fields and Gaussian ring vortex field are first performed to evaluate the reconstruction accuracy and efficiency of the proposed system. Experiments on a circular jet flow are conducted to further validate the velocity measurement accuracy. Results indicate that the particle reconstruction elongation is reduced more than 10 times compared to the single-camera LF-PIV and the reconstruction efficiency is improved at least twice compared to the conventional SART. The accuracy is improved significantly for the ring vortex and 3D jet flow fields compared to the single-camera system. It is therefore demonstrated that the proposed system is capable of measuring the 3D flow field fast and accurately.

Keywords: 3D flow measurement, Particle image velocimetry, Dual light field cameras, Ordered-subset reconstruction algorithm, Reconstruction elongation effect

1. Introduction

With a great desire to reveal the topology of complex unsteady flow structures, continuous efforts have been dedicated to developing three-dimensional (3D) particle image velocimetry (PIV) techniques (e.g., defocusing digital PIV [1,2], tomographic PIV [3,4], synthetic aperture PIV [5,6]) and Lagrangian particle tracking techniques [7,8]. Although these techniques are different in terms of image processing methods, they are all based on conventional imaging, i.e., the flow field is projected to the image sensor through a single lens. In conventional imaging, the propagation directions of the light rays are lost owing to the integral effect of the lens aperture. Therefore, typically multiple cameras (at least 4 or more) are required to capture the flow field from different perspectives for achieving 3D velocity measurement [9]. However, large optical access is required for the multiple-camera system, which may limit its applicability in space-constrained applications such as compressor inlets, turbine inter-stage blades, etc. Thus, it is crucial to achieving 3D flow measurement without modifications to existing perspective views of the applications.

Light field (LF) camera-based systems are alternatives to multiple-camera systems [10,11]. In contrast to conventional cameras, a dense microlens array (MLA) is added in front of the image sensor and enables the LF camera to record the position and direction information of the light rays simultaneously, which contains the full 3D spatial information of the flow field. The volumetric velocimetry of 3D flow can be achieved with the use of a single LF camera along with the 3D-PIV technique.

The single-camera-based LF-PIV technique has been demonstrated in a wide variety of flows including cylinder wakes [12], slot jets [13], conductive flow [14] and ring vortex [15]. Although the lateral and axial components of the test flows can be obtained simultaneously (referred to as 3D-3C), a degraded accuracy is demonstrated in the depth direction compared to the lateral directions [16]. The poor measurement accuracy in the depth direction is due to the elongation effect of the reconstructed tracer particles [17,18]. As the spatial resolution of the single LF camera system is low in the depth direction [19,20], the actual locations of the particles cannot be reconstructed accurately by the tomographic reconstruction algorithms (e.g., Simultaneous/Multiplicative algebraic reconstruction technique, SART/MART [21,22]), thus elongation effects do exist in the reconstruction result.

To eliminate the elongation effect, a pre-recognition (PR) method combined with the SART has been developed based on the line-of-the-sight technique [23]. The PR method identifies the locations of the voxels that contain no tracer particles and sets their intensities as zero in the reconstruction, thereby reducing the elongation effect. However, the performance of the PR method is sensitive to image noises, calibrations and particle seeding concentration. Severe elongations can still be produced at a dense seeding concentration (e.g., >1 particle per microlens). In addition to the reconstruction algorithms, efforts have been made to improve the LF imaging system in terms of increasing the viewing angle and spatial resolution by adding extra LF cameras. Study shows that adding an extra LF camera greatly improves the spatial resolution in the depth direction, but adding a third camera provides a minimal improvement [24]. Therefore, it is demonstrated that the selection of a dual-camera configuration is an optimal choice for improving the spatial resolution and less system complexity compared to the three-camera system. The dual-camera configuration help to mitigate the particle elongation effect, however, the computational time can be increased accordingly. The SART or MART can reconstruct the particle distributions but requires larger

memory storage and longer computation time [25]. This is mainly due to the calculation of the weight matrix required by the reconstruction algorithms. The weight matrix is a large sparse matrix containing the intensity contribution of the discrete voxels to the image pixels [26]. As reported [27], for a weight matrix containing 300×200×200 voxels, 350 GB storage is required only for the non-zero elements in the single-camera configuration. The addition of a second LF camera will double this number. Such a large memory requirement limits the implementation of the tomographic reconstruction on a regular PC. Even on a workstation with large memory storage and a multi-core CPU, the reconstruction of 3D particle distribution requires a longer computational time. To improve computational efficiency, the filtered refocusing (FR) method is used instead of the tomographic algorithm for particle reconstruction [18]. Though the computational cost can be reduced by the FR since the weight matrix is not required, the particle elongation effect is still significant in the reconstruction.

The SART or MART also provide faster convergence but depends on the number of iterations. The ordered subset (OS) technique can be integrated with SART or MART to accelerate the reconstruction process. The main principle of the OS method is to decompose the complete projections into several subsets according to the projection directions and each subset can be used to correct the target voxels' intensities individually. Through the multiple corrections of the subset, the reconstruction convergence can be achieved with fewer iterations and thus the reconstruction process can be accelerated. The memory requirement can also be reduced because the large weight matrix can be split into several pieces corresponding to the subset projections and can be read into the memory one by one.

Compare with the state-of-the-art, the contribution of this study is to develop a dual-camera LF-PIV system integrated with the ordered-subset SART (OS-SART) for accurate and faster measurement of 3D flow velocity. The proposed system is verified by numerical reconstructions of particle fields and a Gaussian ring vortex field and then further validated through experiments on a 3D circular jet flow. The proposed system reduces the particle reconstruction elongation effect significantly and improves the reconstruction spatial resolution and efficiency. A detailed description of the proposed system is given and results obtained from the numerical and experimental study are presented and discussed.

2. Principle of dual-camera LF-PIV

2.1 3D velocity field measurement

In LF imaging, the light rays entering the main lens are firstly focused on the MLA, and then further redirected by the microlens to different pixels on the image sensor. By this process, the positions and directions of the rays that contain the spatial information of the object scene can be recorded by the microlens and pixels, respectively. With the use of the LF rendering methods (e.g., LF refocusing and perspective shift), the 3D spatial information can be retrieved from the LF images. Details about the LF camera architecture and rendering methods can be found elsewhere in [11].

The LF camera is applied to the PIV techniques for 3D flow velocity measurements due to its ability to capture the 3D object scene. Fig. 1 illustrates the working principle of the proposed dual-camera-based LF-PIV technique. The test flow is seeded with tracer particles and illuminated by a double-pulsed laser with high pulse energy. The motions of the particles are captured by the dual camera system from two views. A synchronous controller is used to synchronize the two LF cameras and the pulse laser. The raw LF images are acquired and then preprocessed to remove background

noise associated with the surface reflections. The proposed OS-SART algorithm is then employed to reconstruct the 3D particle distributions. Once the particle volumes are reconstructed, the cross-correlation calculation is performed to estimate the 3D particle displacements.

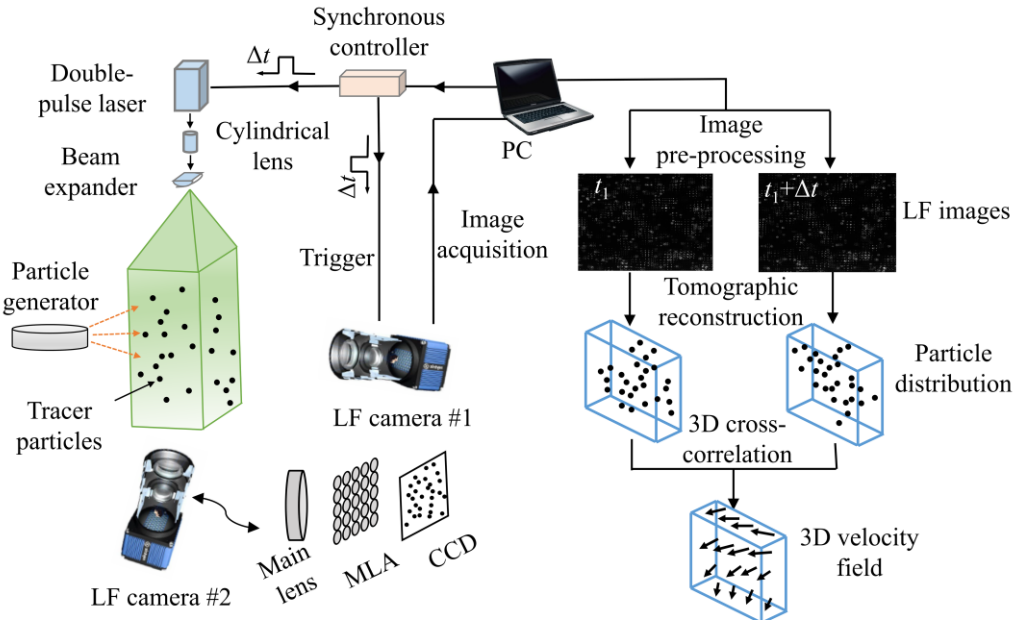

Fig. 1 Principle of dual-camera LF-PIV technique.

2.2 Reconstruction elongation effect

The crucial step of the LF-PIV-based 3D particle reconstruction is to reduce the elongation effect. The particle reconstruction is an inverse problem, which can be mathematically expressed as a set of linear equations,

$$\begin{aligned} &w_{1,1}\cdot E_1 + w_{2,1}\cdot E_2 + \cdots + w_{j,1}\cdot E_j + \cdots + w_{M,1}\cdot E_M = I_1 \\ &w_{1,2}\cdot E_1 + w_{2,2}\cdot E_2 + \cdots + w_{j,2}\cdot E_j + \cdots + w_{M,2}\cdot E_M = I_2 \\ &\vdots \\ &w_{1,i}\cdot E_1 + w_{2,i}\cdot E_2 + \cdots + w_{j,i}\cdot E_j + \cdots + w_{M,2}\cdot E_M = I_i \\ &\vdots \\ &w_{1,N}\cdot E_1 + w_{2,N}\cdot E_2 + \cdots + w_{j,i}\cdot E_j + \cdots + w_{M,N}\cdot E_M = I_N \end{aligned} \tag{1}$$

where E_j denotes the light intensity of the j_{th} discrete voxel in the measurement volume (j is from 1 to total voxel number M), I_i denotes the gray value of the i_{th} pixel on the image sensor (i is from 1 to total pixel number N), and $w_{j,i}$ is the weight coefficient that describes the intensity contribution of the j_{th} voxel to the i_{th} pixel. The grey values of the pixels can be known from the LF image, and the weight coefficients can be calculated by using the volumetric calibration techniques as described in [28,29]. The collection of all the weight coefficients is a large sparse matrix and the order of this weight matrix is usually smaller than the total number of voxels M. As a result, Eq. (1) is undetermined with non-unique solutions. Various algebraic tomographic reconstruction algorithms are used to solve Eq. (1), however, the convergence is different under different optimization criteria [22,30]. For example, in the SART, the minimum norm technique is used to minimize the difference between the image intensity and the projected volume intensity. The projected voxel intensity can be updated by iterations, defined as follows,

$$E_j^{k+1} = E_j^k + \mu \frac{\sum_{i \in N_\beta} \left(\frac{I_i - \sum_{m=1}^{M} w_{m,i} E_m^k}{\sum_{m=1}^{M} w_{m,i}} w_{j,i} \right)}{\sum_{i \in N_\beta} w_{j,i}} \tag{2}$$

where E_j^k denotes the intensity of the j_{th} voxel in the k_{th} iteration, N_β denotes the pixel number under a certain projection angle β, and μ is the relaxation factor.

Although the voxels' intensities are corrected repeatedly through multiple iterations, errors still exist in the reconstruction result. Fig. 2 shows an example of ground truth and reconstructed particle intensity distributions. It can be seen that the total number of non-zero intensity voxels are 3 and 13 for the ground truth and reconstructed particles, respectively, indicating that the reconstruction elongation effect does exist. The elongation length is closely related to the difference between the order of the weight matrix and the number of unknowns in Eq. (1), and a larger difference corresponds to the higher reconstruction errors and hence involves the severe elongation effect. Compared to the single-camera system, the dual-camera system doubles the number of linear equations in Eq. (1) and increases the order of the weight matrix significantly. As a result, the reconstruction errors can be reduced and the particle elongation effect can also be alleviated.

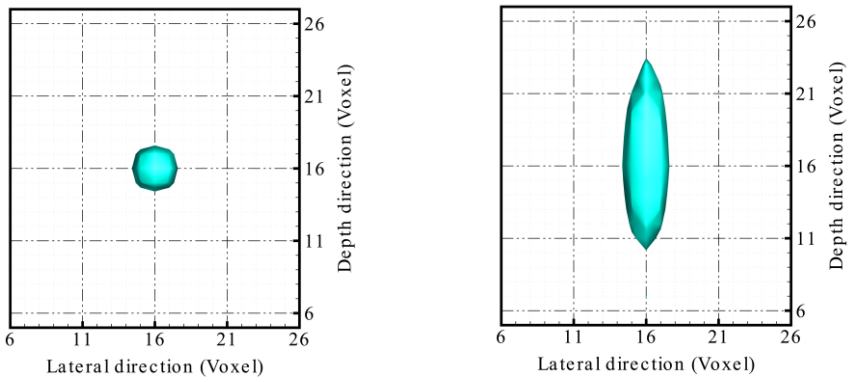

(a) Ground truth (b) Reconstruction

Fig. 2 Comparison of the actual and reconstructed particle intensity distribution.

The mitigation of the elongation effect by an additional LF camera can also be interpreted from the viewing angle of the imaging system (namely tomographic angular α [9]). For the single-camera system, the α is limited due to the finite pupil diameter of the main aperture. As a result, the elongation of the particle is significant, as illustrated in Fig. 3(a). In contrast, adding an extra LF camera increase the α notably as shown in Fig. 3(b). It can be seen that the elongation effect can mostly be alleviated with the intersections of the line-of-the-sights of two cameras, also the shape of the reconstructed particle is much closer to the actual particle. Therefore, the larger α offered by the dual-camera system provides higher accuracy of particle reconstruction.

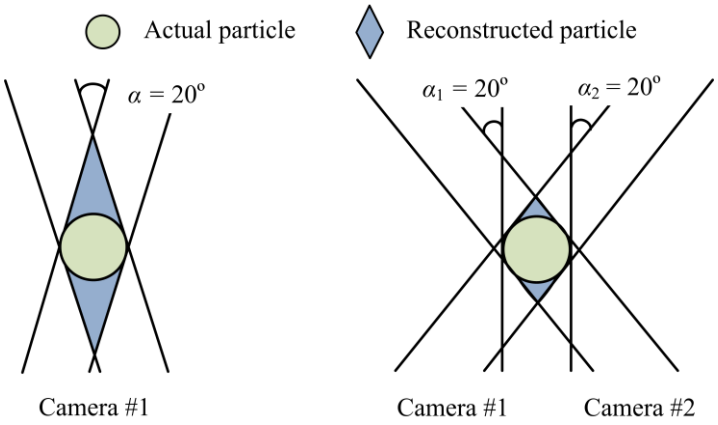

(a) Single camera, $\alpha = 20°$ (b) Dual cameras, $\alpha_1 = \alpha_2 = 20°$

Fig. 3 Reconstruction elongation effect caused by the limited viewing angle of the imaging system.

3 Ordered-subset SART

In 3D particle reconstruction, the weight matrix requires a large memory space to store, which leads to a high computational cost. To reduce the burden of memory storage and accelerate the reconstruction process, the OS method is integrated with the SART as discussed in Section 2.2. The OS method increases the convergence rate of SART through correctional updates within the subsets projection data. In particular, the complete projection data is divided into subsets according to the projection directions and then used to correct the voxels intensities individually. As a result, faster correction on the voxels intensities can be achieved in each iteration compared to directly using the complete projection data [31]. Fewer iterations are required to reach the desired reconstruction quality and thus the reconstruction efficiency is improved. Fig. 4 illustrates an example of the faster convergence achieved by the proposed OS-SART by solving Eq. (1). The reconstruction error (ε) is defined as

$$\varepsilon = \sqrt{\sum_{j=1}^{M} \left(E_{j,r} - E_{j,a} \right)^2} \tag{3}$$

where $E_{j,r}$ and $E_{j,a}$ denote the reconstructed and actual intensity of the j_{th} voxel, respectively and M is the total voxel number. It can be seen that though the convergence of SART and OS-SART is similar, the convergence requires 125 and 75 iterations, respectively. The OS-SART can achieve particle reconstruction with fewer iterations.

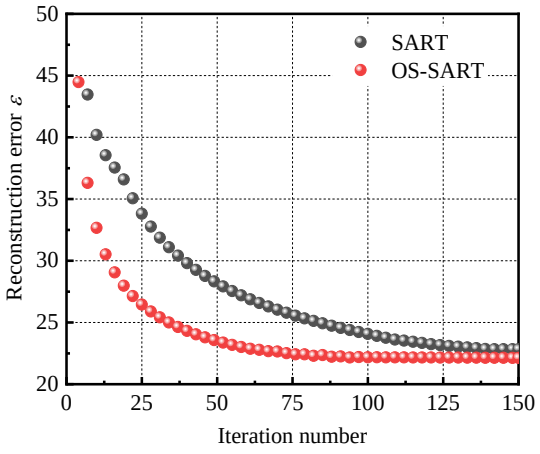

Fig. 4 Variation of reconstruction error with iteration number in SART and OS-SART methods.

Another advantage of applying the OS method is to release memory space. Since the corrections of voxels' intensities are made in order of the subsets, the weight matrices corresponding to different subsets projection data can be read into the memory one by one, i.e., a weight matrix is cleared before loading the next one. In this way, the required memory space can be reduced significantly compared to using the complete projection data in the conventional SART.

However, it is crucial to consider the order subsets of SART carefully to improve the reconstruction efficiency. As reported [31], the balanced subsets (i.e., each subset data contains the projections from the same number of directions) are recommended for faster convergence and high noise resistance of the reconstruction. In LF imaging, since a fixed sub-aperture position corresponds to a certain viewing perspective, the balanced subsets of projection data can be constructed by extracting the sub-aperture images from a LF raw image. Specifically, as the light rays that pass through a fixed sub-aperture can only hit the same pixels covered by each microlens (e.g., in Fig. 5, the rays from sub-apertures #1 and #5 can only hit pixels #1 and #5, respectively), therefore, a sub-aperture image can be acquired by extracting the same pixel behind each microlens [32]. From this perspective, the number of the subset (N_s) that are divided from the LF raw image can be calculated as,

$$N_s = \frac{N_p^{\,2}}{N_d} \tag{4}$$

where N_p denotes the number of pixels covered by each microlens in the x and y-direction (e.g., N_p = 5 in Fig. 5) and N_d denotes the number of projection directions in each subset. For the dual LF camera system, the ordered subsets of each camera can be constructed separately and thus the corrections of voxels intensities are made $2N_s$ times in each iteration of SART.

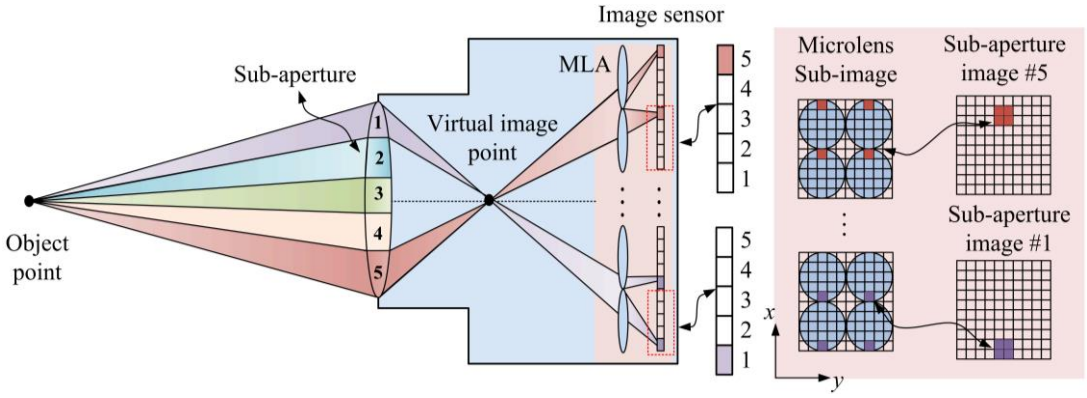

Fig. 5 Construction of the ordered subset data from LF images for OS-SART reconstruction.

In addition to the subset construction, the input of ordered subsets also affects the reconstruction efficiency. To provide the projections from different views for faster corrections of the voxels' intensities, the subsets extracted from the LF images of two cameras are employed to the SART alternately. The implementation procedure of the OS-SART for the dual LF camera system is illustrated in Fig. 6.

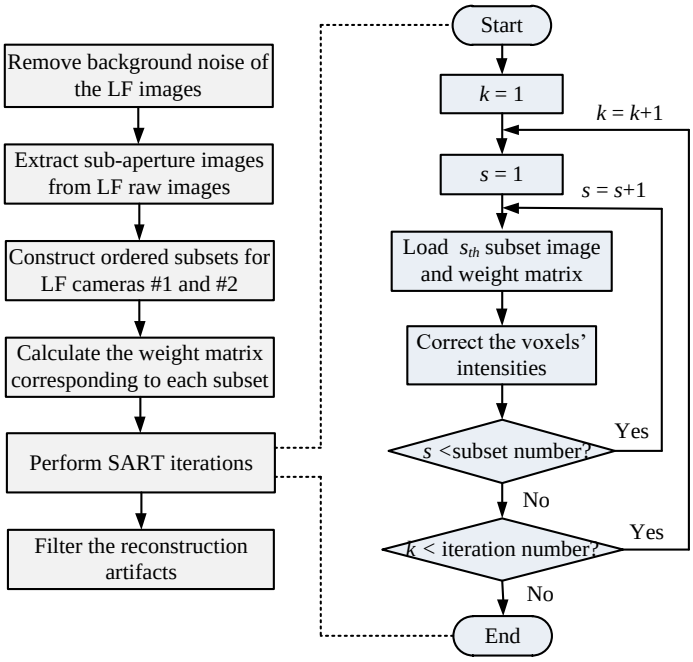

Fig. 6 Implementation procedure of the OS-SART for 3D particle reconstruction of dual-camera LF-PIV.

4. Numerical verification

To verify the particle reconstruction accuracy and efficiency achieved by the dual-camera system along with the OS-SART, numerical reconstructions are conducted on the particle fields and a Gaussian ring vortex via synthetic LF images. Since there is no image noise, lens distortions and calibration errors in this synthetic test, the velocity measurement error caused by the particle reconstruction elongations can be well evaluated. The numerical settings of the LF camera parameters for particle field and ring vortex reconstructions are the same as experimental settings and are listed in Table 1.

Table 1: Optical parameters of the LF camera

Parameter	Symbol	Value
Configuration	-	Unfocused type
A magnification ratio of the main lens	m	-1
Focal length of the main lens	F_m	100 mm
f-number of the main lens	$F/\#$	4
Focal length of the microlens	f_m	0.8 mm
f-number of microlens	$f/\#$	8
Microlens geometry	-	Square
Microlens pitch	p_m	0.1 mm
Number of microlenses	n_x, n_y	251×251
Pixel size	p_x	5.5 μm
Number of pixels	N_x, N_y	2352×1768
Number of cameras	-	2
Camera separation angle	θ	90°

4.1 Particle field reconstruction

Synthetic LF images are generated by the light ray tracing technique based on geometrical optics. Specifically, the measurement volume is discretized as a 3D array of cubic voxels in x, y and

z directions with intensity $E(x, y, z)$. A large number of light rays from the voxels [$E(x, y, z) > 0$] are traced to the image sensor through the ray transfer matrix and their intensity contributions on the pixels are accumulated to form the image. By setting the number of voxel with intensity above 0, different particle seeding concentrations can be simulated. More details about synthetic image generation can be found elsewhere in [33]. Examples of synthetic LF images at particle concentrations (C) of 0.1 and 1 particle per microlens (ppm) are shown in Fig. 7.

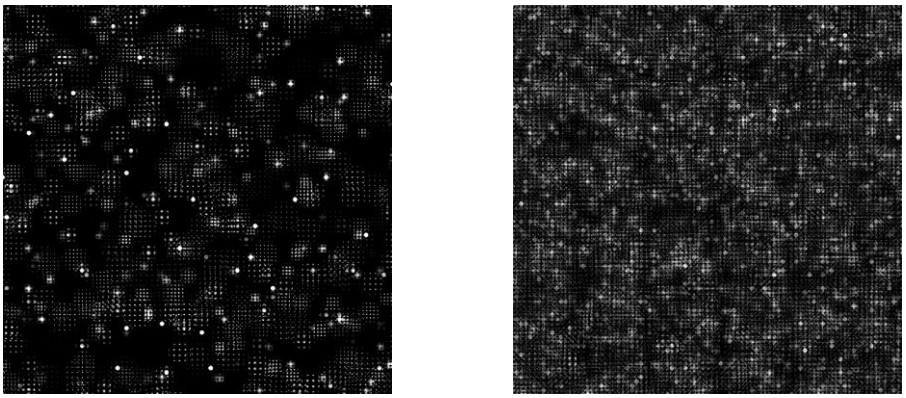

(a) C = 0.1 ppm (b) C = 1 ppm

Fig. 7 Examples of synthetic LF image at particle concentrations (C) of 0.1 and 1 ppm.

Figure 8 illustrates the dual LF camera system and the world coordinate of the measurement volume. The optical axes of two LF cameras are set as orthogonal for a large viewing angle of the imaging system and therefore higher reconstruction accuracy [15]. The z and y-axis of the measurement volume are parallel to the optical axes of LF cameras #1 and #2, respectively. At first, the reconstruction of a single particle is performed. The measurement volume with the size of 3 mm×5 mm×24 mm is discretized as 30×50×240 cubic voxels and the center is aligned with the focal points of two cameras. The reconstruction performance is compared between the conventional SART and OS-SART for both single and dual-camera systems. The pre-recognition SART (PR-SART) proposed in [23] is also performed in the single-camera system. In each algorithm, 1000 iterations are performed with a relaxation factor of 1 to verify the convergence.

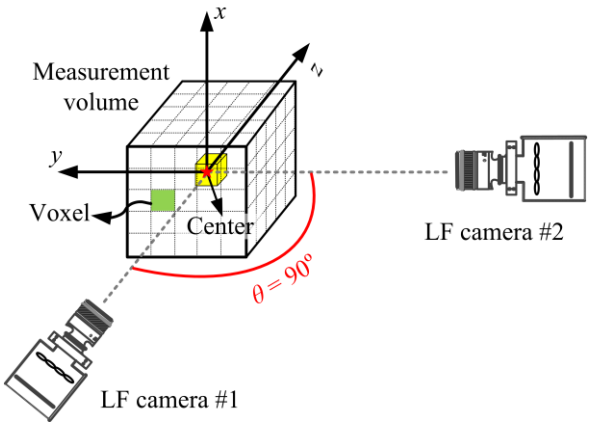

Fig. 8 Illustration of the defined world coordinates and viewing angles of two LF-cameras.

The reconstruction of a single particle located at the focal point of two LF cameras (i.e., (x, y,

z) = (0, 0, 0)) is demonstrated in Fig. 9. It can be seen that the reconstructed particles via a single LF camera (camera #1) are elongated along the optical axis direction both for the conventional SART and OS-SART [Fig. 9(b) and (c)]. The use of the PR-SART mitigates the elongation length [Fig. 9(d)], but it is still 6 times larger than the ground truth [Fig. 9(a)]. The dual LF camera system overcomes this problem effectively. Both the SART and OS-SART can reconstruct the particle accurately without elongations in the dual-camera system [Fig. 9(e) and (f)].

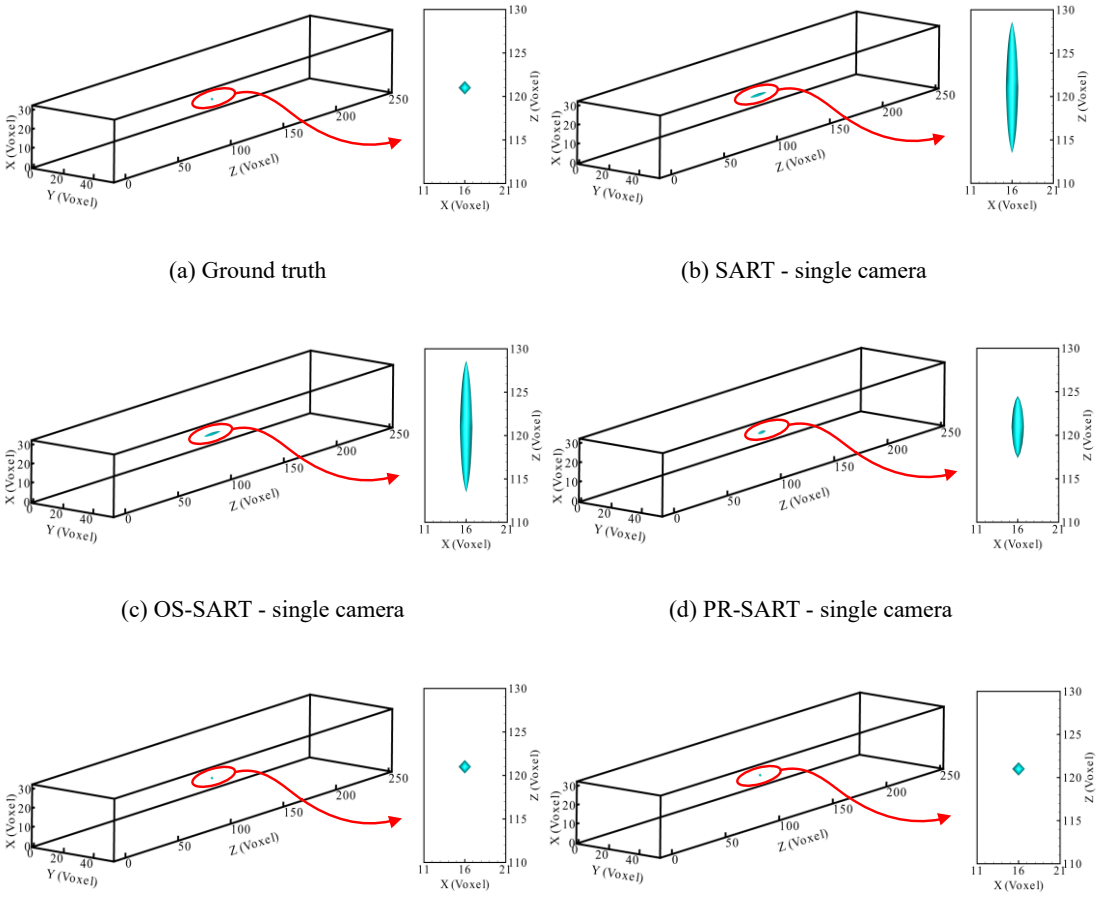

(a) Ground truth (b) SART - single camera

(c) OS-SART - single camera (d) PR-SART - single camera

(e) SART - dual cameras (f) OS-SART - dual cameras

Fig. 9 Reconstruction result of a single particle located at focal point of LF camears.

The particle elongation length can be characterized quantitatively by the full-width at half-maximum (FWHM) [34] intensity of the reconstructed particle. For example, the voxel intensity of the reconstructed particle [as shown in Fig. 9(c)] along the z-direction is illustrated in Fig. 10(a). It can be seen that the intensity presents Gaussian distribution and the corresponding FWHM is 1 mm (10 voxels). Fig. 10(b) depicts the FWHM of the reconstructed particles at different depths. Note that, the depth herein is the distance from the particle to the focal point of the LF camera #1. For LF camera #2, the particle is always on its focal point. This setting is due to that the dual cameras are perpendicular to the measurement volume and thus the variation of the FWHM with the depths of camera #1 and #2 will be the same. From Fig. 10(b), it can be seen that the dual LF camera system helps to reduce the reconstruction elongation significantly, even without the pre-recognition process. In the depth of -10 mm < z < 10 mm, the mean FWHM of the particles reconstructed by OS-SART in single and dual camera systems are 1.83 mm and 0.1 mm, respectively. Therefore it indicates that

the reconstruction spatial resolution has been improved by more than 10 times by the dual LF camera system compared to the single LF camera system.

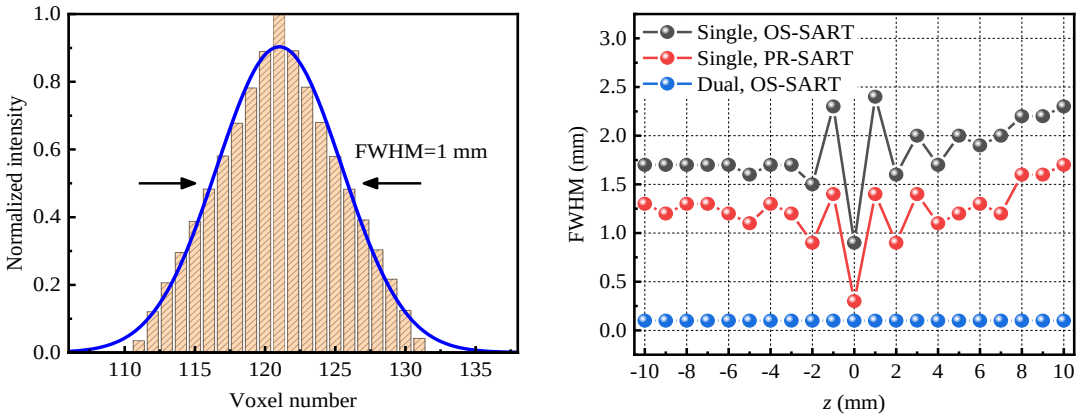

(a) Calculation of FWHM (b) Variation of FWHM with depths

Fig. 10 Characterization of particle elongation (FWHM) and its variation with particle depth location. The positive and negative depths (z) correspond to the far-focal and near-focal zones, respectively.

In the LF-PIV, the reconstruction of a single particle can provide the upper limit of reconstruction resolution. However, the single particle is an ideal case that does not consider the effects of the surrounding particles. To take this effect into account, the numerical reconstruction of multiple particle fields under different C is performed. The size of the measurement volume that contains the multiple particles is 10 mm×10 mm×10 mm and it is discretized as 100×100×100 voxels. Tracer particles are randomly seeded in the measurement volume at different C.

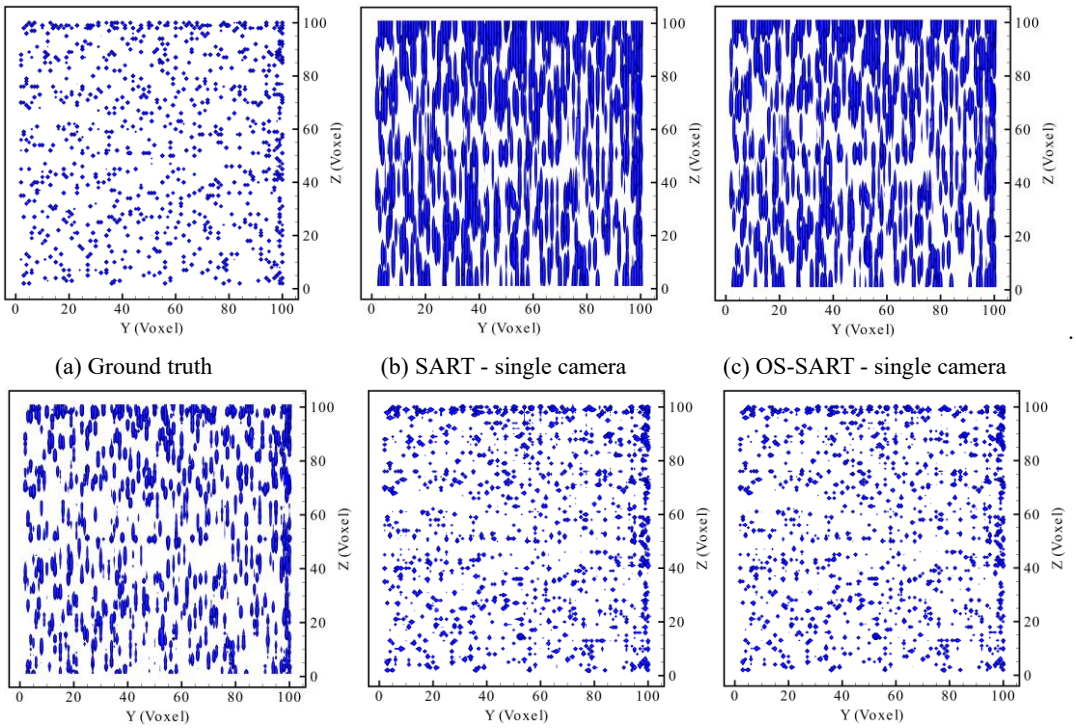

(a) Ground truth (b) SART - single camera (c) OS-SART - single camera

(d) PR-SART - single camera (e) SART - dual cameras (f) OS-SART - dual cameras

Fig. 11 Reconstructed multiple particle fields at C = 0.1 ppm achieved by single and dual camera systems.

Figure 11 shows the reconstructed distributions of the multiple particle field at C = 0.1 ppm. For better illustration, the reconstructed particles in the entire measurement volume are projected to the y-z slices. It can be observed that for the single-camera system [Fig. 11(b) and (c)], the reconstructed particles are trapped to each other due to the severe elongations for both SART and OS-SART and the particle clusters span the entire volume along the depth direction. It is conceivable that if this reconstruction is used in the cross-correlation calculation, significant errors will occur in the velocity measurement. Though the PR-SART partially alleviates the elongations [Fig. 11(d)], the depths of the reconstructed particles still cannot be accurately resolved. In contrast, the elongation effects are reduced significantly by using the dual-camera system [Fig. 11(e) and (f)] and the reconstructed particle distribution is much closer to the ground truth [Fig. 11(a)].

The accuracy of the reconstructed multiple particle field is quantitatively evaluated by the reconstruction quality factor (Q) [35] defined as,

$$Q = \frac{\sum E(x,y,z) \cdot E_0(x,y,z)}{\sqrt{\sum E(x,y,z)^2 \cdot \sum E_0(x,y,z)^2}} \tag{5}$$

where $E(x, y, z)$ and $E_0(x, y, z)$ denote the reconstructed and actual intensity distributions, respectively. Q is between 0 and 1, and a larger Q corresponds to a higher reconstruction accuracy. It is reported [36] that the Q should be larger than 0.75 to ensure that the reconstruction artifacts (e.g., ghost particles, particle elongations) will not affect the error level in the cross-correlation analysis. Fig. 12 illustrates the variations of Q with particle concentrations in single and dual LF camera systems. Note that the Q of conventional SART is not depicted in this figure because it is same with OS-SART with 1000 iterations. The reconstruction accuracy is much higher for the dual-camera system compared to the single-camera system. Although Q gradually decreases as the concentration gets denser, it is always higher than 0.75 in the dual-camera system, indicating that accurate particle reconstruction can be achieved even at a relatively dense concentration.

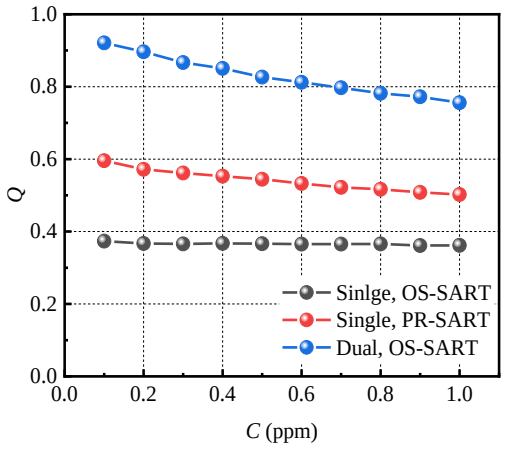

Fig. 12 Variation of Q with particle concentration (C) in single and dual-camera systems.

To illustrate the advantage of the OS-SART compared to the conventional SART, the variation of Q with the iterations is depicted in Fig. 13(a). Noticeably, the Q converges at the same level for both algorithms but requires different iterations. For C = 0.1 and 0.5 ppm, the OS-SART requires about 400 iterations to converge, while the conventional SART requires around 800 iterations. Taking Q = 0.75, the acceleration ratio τ of the OS-SART (i.e., the ratio of computation time of

SART to OS-SART) is depicted in Fig. 13(b). It can be seen that the reconstruction process is accelerated at least twice at a particle concentration of 0.1 to 1 ppm, indicating that the OS-SART can improve the reconstruction efficiency significantly. Additionally, the memory space required by the OS-SART is only 1/12 of the conventional SART, which enables a regular PC to perform 3D particle reconstruction by the dual-camera LF-PIV system.

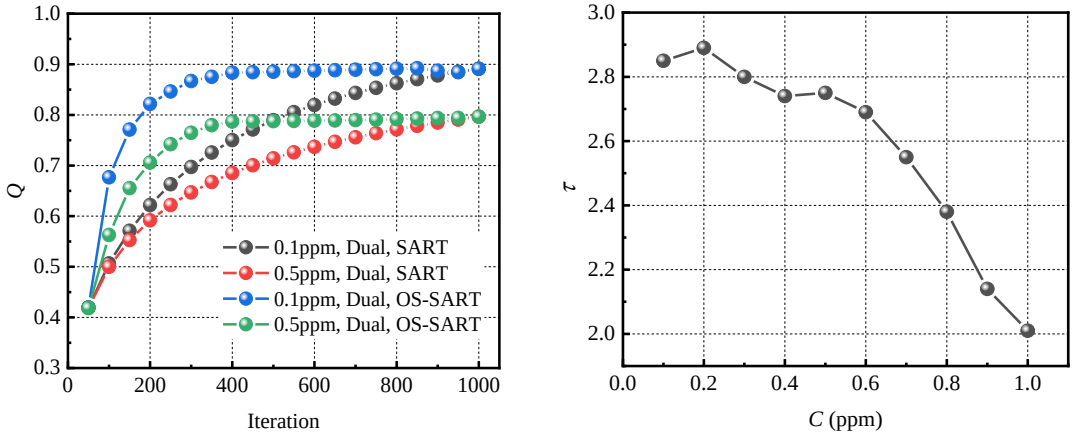

(a) Variation of Q with iterations of SART and OS-SART (b) Acceleration ratio of OS-SART relative to SART

Fig. 13 Q with iterations of SART and OS-SART algorithms and the acceleration ratio of the OS-SART.

4.2 Gaussian ring vortex field reconstruction

For this test, a 14 mm×14 mm×7 mm measurement volume of ring vortex is imaged by the dual LF camera system (as illustrated in Fig. 8) and discretized as 140×140×70 cubic voxels for reconstruction. The particles are randomly distributed in the measurement volume and displaced using the analytical equation for the Gaussian ring vortex [12]. The LF images correspond to different particle distributions that are subsequently generated.

To reconstruct the particle distributions, 400 iterations are performed in the SART, PR-SART and OS-SART with a relaxation factor of 1. The reconstructed particle volumes are then fed into the cross-correlation algorithm to estimate the 3D particle displacement field. In the cross-correlation calculation, the window size of 16×16×16 voxels with 50% overlap is considered. To generate the actual particle displacement field, a pair of volumes that contains the particles at exact locations is also processed by the cross-correlation algorithm.

The 3D visualizations of the reconstructed vorticity fields at C = 1 ppm are illustrated in Fig. 14. For ease of comparison, the magnitude of the vorticity iso-surface is set as 0.2 voxels/voxel in this figure. The dense vectors around the vortex present the 3D displacement field. Compared to the ground truth [Fig. 14(a)], significant distortions of the vorticity iso-surface can be seen in the reconstructions achieved by the single camera, no matter which reconstruction algorithm is used [Fig. 14(b)-(d)]. Many spurious displacement vectors are generated (marked in red dot ellipses). Though the reconstruction of SART using the dual-camera system [Fig. 14(e)] appears better, various spurious displacements around the vortex ring still exist due to a lack of iterations. In contrast, the reconstruction of OS-SART [Fig. 14(f)] appears much closer to the ground truth and the tour shape is well reconstructed. The velocity vectors are generally concentrated near the vortex ring, indicating that most of the spurious vectors have been removed. This further indicates that the OS-SART with the dual-camera system can achieve accurate reconstruction with fewer iterations compared to the conventional SART.

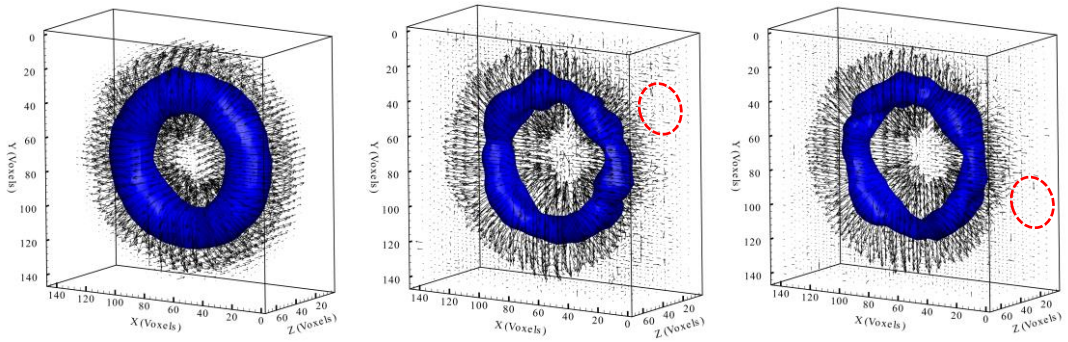

(a) Ground truth (b) SART - single camera (c) OS-SART - single camera

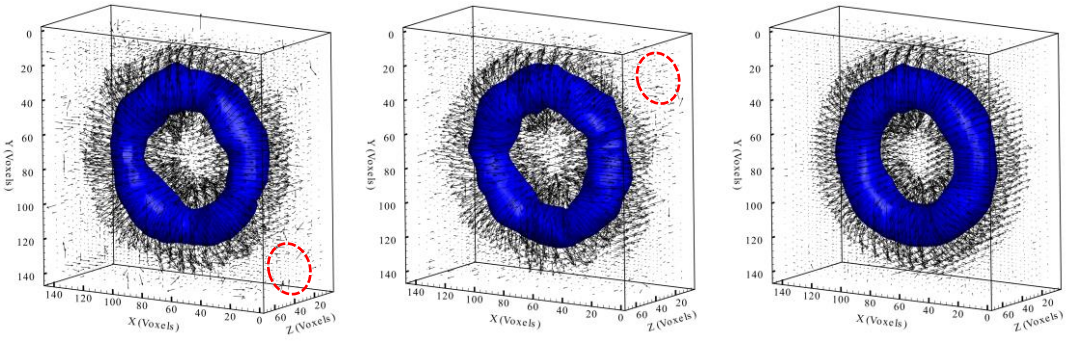

(d) PR-SART - single camera (e) SART - dual cameras (f) OS-SART - dual cameras

Fig. 14 Displacement and vorticity fields of the Gaussian ring vortex reconstructed by single and dual LF cameras. Displacement is shown by the arrow and vorticity is shown by the iso-surface.

Further comparisons have been performed by extracting the displacement field on 2D slices from the 3D data. Figs. 15 and 16 illustrate the *v* component (i.e., displacement in the *y* direction) on the central *y*-*z* slice and the *w* component (i.e., displacement in the *z* direction) on the central *x*-*y* slice, respectively. From Figs. 15 (b)-(c) and Figs. 16 (b)-(c), it can be seen that the *w* component is closer to zero for both the SART and OS-SART achieved by the single camera system. This can be interpreted as the severe elongation effect dampens the depth displacement component in the cross-correlation calculation [12]. The PR-SART partially alleviates the elongation effect and the *w* component is visible in the reconstruction results [Figs. 15(d) and 16(d)], although some defects still exist. More accurate reconstruction results of the *w* component can be achieved by the dual-camera system. Compared to the conventional SART [Figs. 15(e) and 16(e)], a higher similarity with the ground truth [Figs. 15(a) and 16(a)] can be seen achieved by the OS-SART [Fig. 15(f) and 16(f)]. Both the symmetric vortices on the *y*-*z* slice and the *w* component on the *x*-*y* slice are reconstructed accurately.

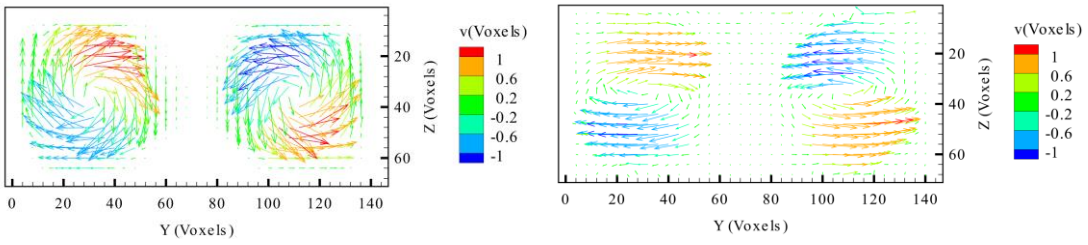

(a) Ground truth (b) SART - single camera

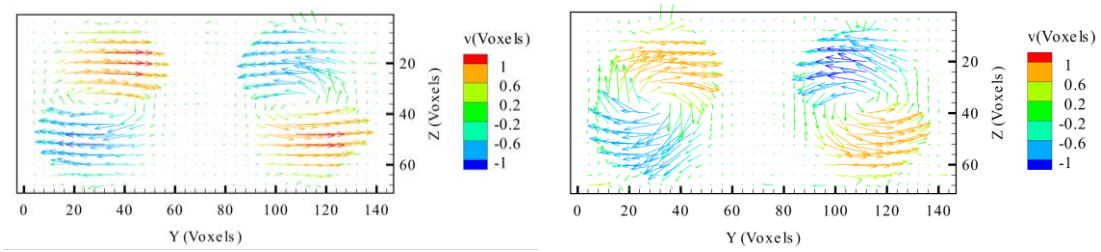

(c) OS-SART - single camera (d) PR-SART - single camera

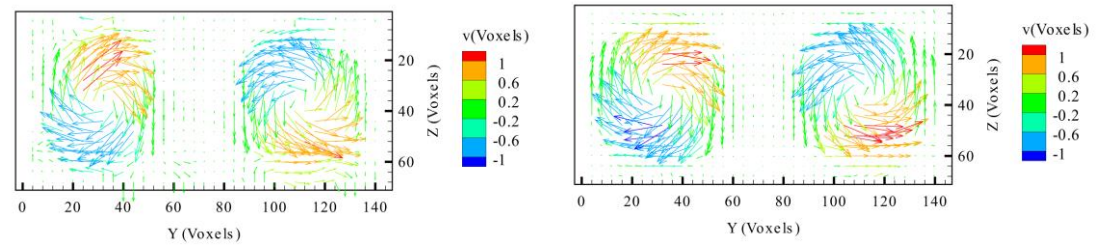

(e) SART - dual cameras (f) OS-SART - dual cameras

Fig. 15 Displacement field of Gaussian vortex on the central *y*-*z* slice (*x* = 70 voxels) reconstructed by single and dual LF cameras. The contour shows the magnitude of displacement *v* component.

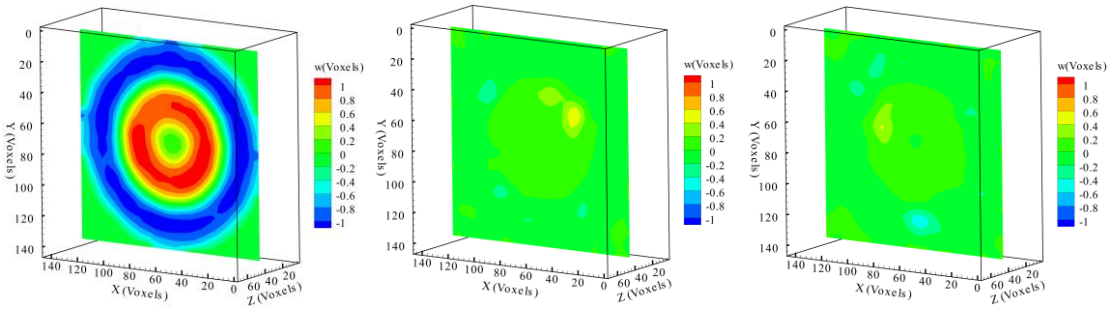

(a) Ground truth (b) SART - single camera (c) OS-SART - single camera

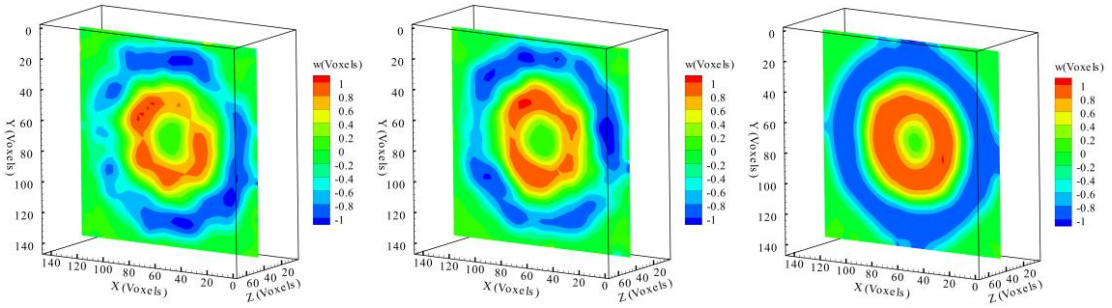

(d) PR-SART - single camera (e) SART - dual cameras (f) OS-SART - dual cameras

Fig. 16 Displacement *w* component on central *x*-*y* slices (*z* = 35 voxels) reconstructed by single and dual LF cameras. The contour shows the magnitude of the *w* component.

The reconstruction accuracy of the displacement field is evaluated quantitatively by calculating the mean displacement error (σ) defined as,

$$\sigma = \frac{\sum_{i=1}^{N_i} \left| V_{i,r} - V_{i,t} \right|}{N_i} \tag{6}$$

where $V_{i,r}$ is the reconstructed i_{th} displacement component, $V_{i,t}$ is the ground truth known from the analytic solution [12] and N_i is the total number of the displacement vector. Fig. 17(a) and (b) illustrate the mean errors of lateral displacement component (v) and depth component (w) at different C, respectively. It can be found that the measurement accuracy of v achieved by the single and dual-camera systems is close. But there is a significant difference in w. Specifically, in the single-camera system, the error (σ_w) of SART and OS-SART is around 0.3 and 0.27 voxels, respectively. The PR-SART outperforms in the sparse seeding cases but has a similar accuracy when the concentration exceeds 1.4 ppm. The dual LF camera system significantly improves the measurement accuracy of the w component. For the OS-SART method, the error σ_w decreases noticeably and reaches the same level as σ_v (smaller than 0.1 voxels), whereas the error σ_w of conventional SART is relatively higher at different concentrations due to the lack of iterations.

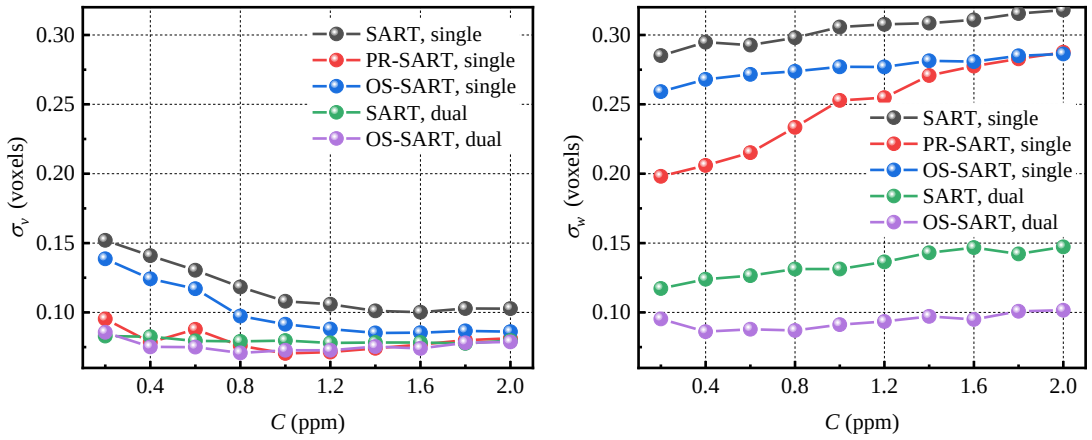

(a) Mean error of lateral v component (σ_v) (b) Mean error of depth w component (σ_w)

Fig. 17 Mean error of the displacement errors at different concentrations reconstructed by single and dual cameras.

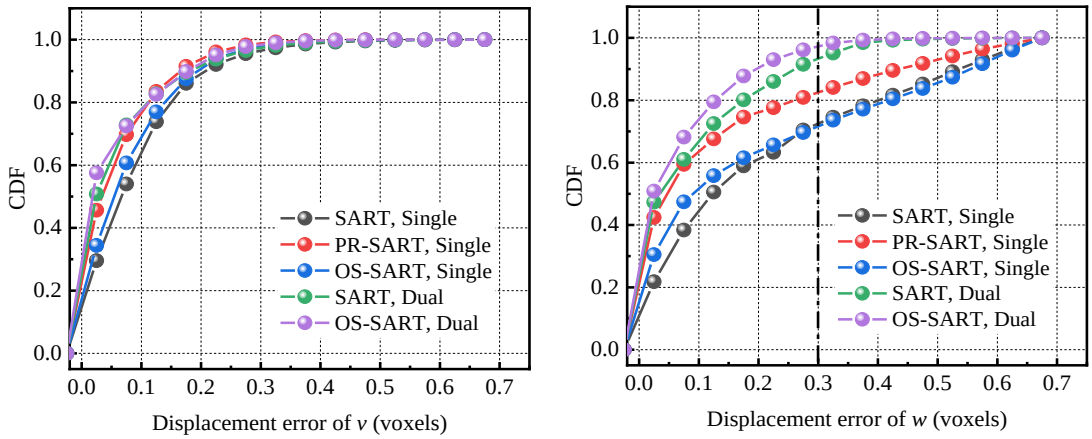

(a) v component (b) w component

Fig. 18 Cumulative distribution function of the displacement errors reconstructed by single and dual LF cameras.

Fig. 18 depicts the cumulative distribution function (CDF) of the v and w component errors at a seeding concentration of 1.6 ppm. It can be seen from Fig. 18(a) that the measurement accuracy of lateral component v is approximate for the single and dual-camera system. The percentage of v component with an error smaller than 0.3 voxels is about 97%. However, there is a significant difference in depth component w [Fig. 18(b)]. For the dual-camera system, the percentage of w

components with an error smaller than 0.3 voxels is about 91% and 96% for SART and OS-SART, respectively. Whereas, for the single-camera system, the accuracy is lower than 82%. It indicates that the dual-camera system along with the proposed OS-SART provides better measurement accuracy.

5. Experiments on a 3D circular jet flow

5.1 Experimental setup

Experiments were carried out on a 3D circular jet flow to validate the dual-camera LF-PIV system along with the OS-SART. Fig. 19 illustrates the experimental setup. The compressed air is stored in the gas tank at constant pressure (0.6MPa) and supplied into the tracer particle generator to blow up the tracer particles (BAMEU2+ particles, mean diameter of 5 μm with a density of 3.17 g/cm^3). The gas tank also connects to an electrical heater, which is used to heat the air. The air from the particle generator and the heater are mixed and ejected from the circular nozzle. The diameter of the nozzle is D = 18 mm, and it is installed about 300 mm away from the bottom surface of the burner to reduce the influence of the wall on the flow field. The airflow rates are fixed at 210 L/min, corresponding to the Reynolds number of $\mathrm{Re}_D = 1.6\times10^4$ based on the bulk velocity v_0 in the nozzle and the nozzle diameter D. The air temperature is kept at 298 K.

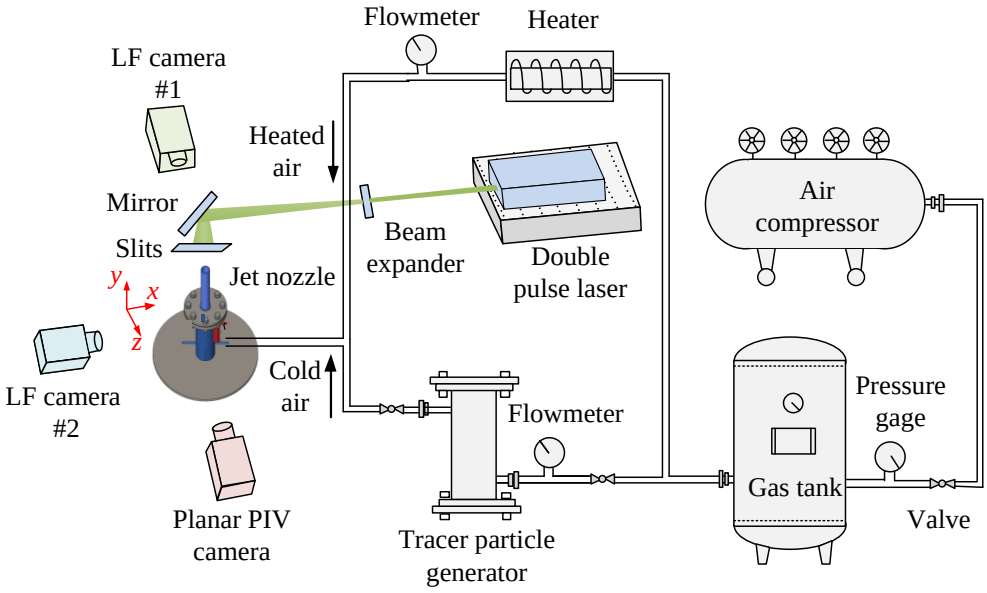

Fig. 19 Schematic of the experimental setup of the circular jet flow.

To measure the 3D jet flow, a double-pulsed Nd: YAG laser (energy of 200 mJ, wavelength of 532 nm) equipped with a beam expander is used to illuminate the tracer particles from the top of the nozzle. Two slits are added in the path of the laser light sheet to create a sharply illuminated volume. With the optical settings listed in Table 1, a measurement volume of 13 mm (0.72D in the x direction) × 10 mm (0.55D in the y direction) × 12 mm (0.67D in the z direction) can be captured by the dual LF cameras whose optical axes are orthogonal to each other.

Figure 20 illustrates the nozzle geometry and position of the measurement volume. From the perspective of LF camera #1, the bottom of the field of view (FOV) is 1.38D upstream of the nozzle outlet, and the center of the FOV is about 0.33D away from the nozzle centerline. From the

perspective of LF camera #2, the height of the FOV is the same as that of LF camera #1, and the center of the FOV is aligned with the nozzle centerline. Fig. 21 gives an example of instantaneous LF raw images captured by dual LF cameras. A total of 200 image pairs are recorded by each LF camera for generating the time-averaged velocity field. To reconstruct the 3D particle distributions, the cuboid measurement volume is discretized as 130×100×120 voxels with a spatial resolution of 0.1 mm×0.1 mm×0.1 mm. The OS-SART algorithm is employed to reconstruct the particle distributions. Based on the simulation results, 400 iterations are performed with a relaxation factor of 1.0. The reconstructed particle volume pairs are subsequently processed by the 3D cross-correlation algorithm with the interrogation volume size of 16×16×16 voxels and an overlap of 50%, returning 12×16×15 velocity vectors with a spatial resolution of 1.6 mm×1.6 mm×1.6 mm.

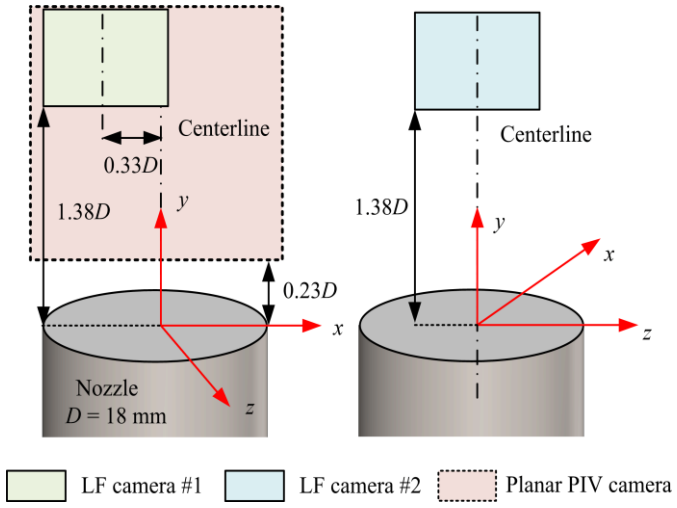

Fig. 20 Nozzle geometry and measurement volume position.

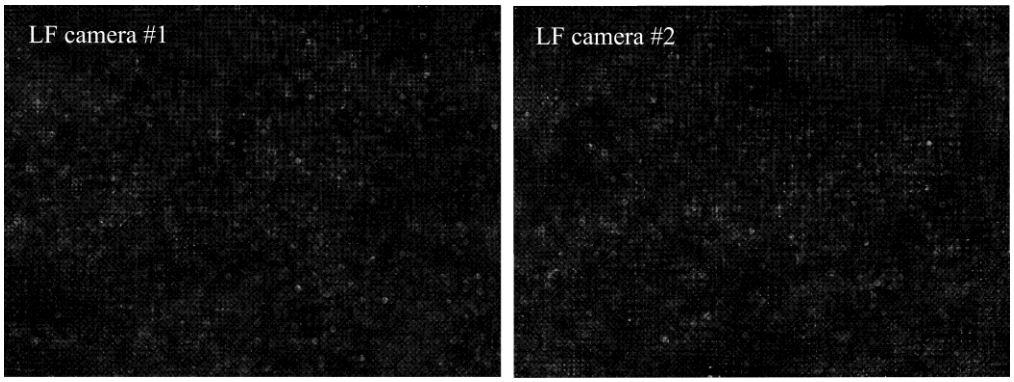

Fig. 21 An example of instantaneous LF raw images captured by dual LF cameras

In addition to the LF-PIV, the planar PIV measurements are also carried out in a similar configuration, as illustrated in Figs. 19 and 20. The planar PIV measurements are used for comparison and quantitative evaluation of the LF-PIV performance. In this study, a conventional camera is employed in the planar PIV which is focused on the central depth of the nozzle (in the z-direction). A FOV of $1.4D \times 1.7D$ is captured with the magnification ratio of the lens set as -0.33. As shown in Fig. 20, the bottom of the FOV is $0.23D$ higher than the nozzle outlet (in the y-direction), and the center is aligned with the nozzle centerline (in the x-direction). With the time interval between two frames set as 100 μs, a particle displacement of 60 pixels is achieved. In the cross-

correlation calculation, the initial and final window sizes of 256×256 pixels and 32×32 pixels are used for achieving the velocity field measurement with a spatial resolution of 0.53 mm×0.53 mm. A total of 350 instantaneous velocity fields are calculated for producing the time-averaged velocity data with high fidelity.

5.2 Results and discussions

Fig. 22(a) and (b) show the time-averaged streamwise velocity distribution measured by single LF and dual LF camera systems, respectively (contour shows the magnitude). A common finding is that the streamwise velocity on the *x*-*y* slice gradually decreases from the centerline ($x/D = 0$) to the edge (x/D = -0.65) of the nozzle. However, there is an unperceivable difference on the *x*-*z* slice. Specifically, the velocity gradient is shown in the measurement achieved by the dual LF camera system, whereas it is disappeared for the single-camera system. Considering that the nozzle geometry is axisymmetric, the streamwise velocity distribution along the *x* and *z*-directions should be the same. Therefore, the velocity gradient shown in the *x*-*z* slice is the truth. The poor accuracy in the *z*-direction achieved by the single-camera system is due to the reconstruction elongation effect, while this effect has been significantly reduced by the dual-camera system and therefore achieves accurate results.

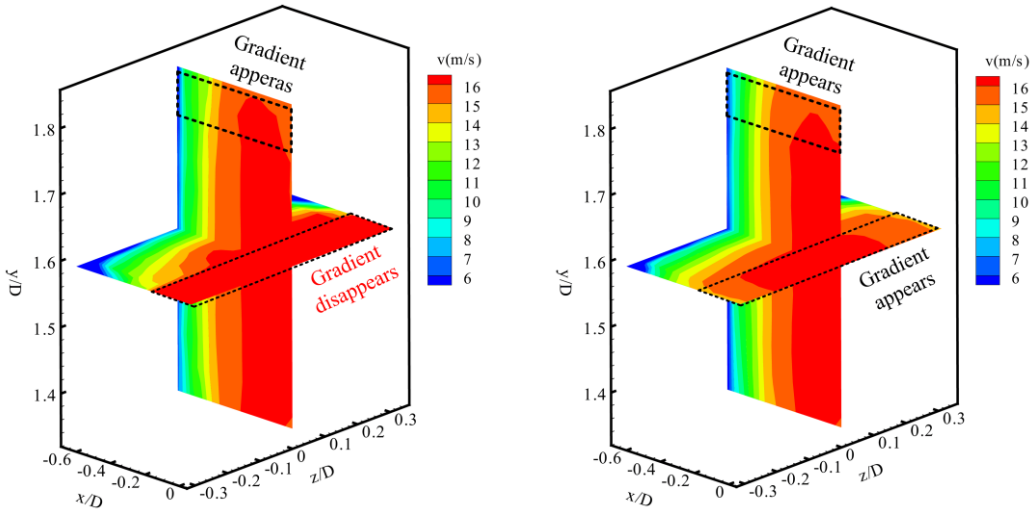

(a) Single LF camera (b) Dual LF cameras

Fig. 22 Time-averaged streamwise velocity distribution reconstructed by single and dual LF camera systems.

The 2D slices at $z/D = 0$ are extracted from the 3D velocity data measured by the single and dual LF camera systems, and compared with the planar PIV measurement result, as shown in Fig. 23. The result achieved by the planar PIV [Fig. 23(a)] shows an axisymmetric distribution of streamwise velocity along the radial direction of the nozzle (*x*). The high bulk velocity is demonstrated in the core region of the jet flow ($-0.25 < x/D < 0.25$) and decreases gradually from the centerline to the edges. The streamwise velocity in the core region keeps a constant of around 16m/s at different axial locations (*y*), but the velocity outside the core region decreased sharply from upstream to downstream of the nozzle outlet. This can be interpreted that due to the fluctuations of the gas parcels around the jet boundary, the exchange of mass and momentum between the jet flow and surrounding static air has occurred. The airflow outside the core region is affected by jet diffusion and gradually gets slower due to the decreased momentum. With the development of the

jet flow from the upstream to the downstream, the core region shrinks accordingly, until the energy of the jet flow is completely dissipated.

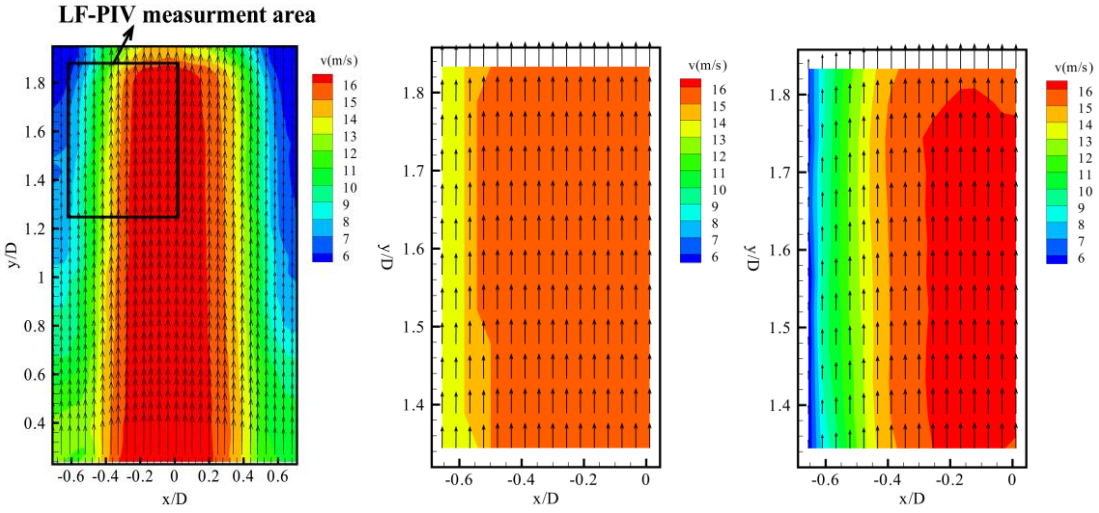

(a) Planar PIV (b) Single LF camera (c) Dual LF cameras

Fig. 23 Time-averaged streamwise velocity distribution on the central depth of the measurement volume ($z/D = 0$) measured by (a) planar PIV, (b) single LF camera (#2), and (c) dual LF cameras.

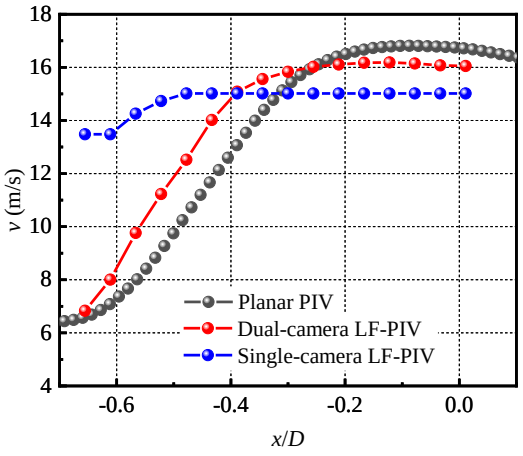

Fig. 24 Time-averaged streamwise velocity distribution along the radial direction (x) measured by the LF-PIV and planar PIV. The result is averaged along the axial direction (y).

Due to the limited FOV of the LF cameras, the measurement of the LF-PIV can only be compared with a sub-region of the planar PIV [marked as a black box in Fig. 23(a)]. The measurement result achieved by the dual LF camera system [Fig. 23(c)] is almost similar to the planar PIV. The velocity gradient has been shown from 16m/s to 6m/s. While the decrease of the velocity along the radial direction (x) cannot be found in the measurement achieved by the single LF camera [Fig. 23(b)]. The quantitative comparison of the time-averaged streamwise velocity distribution along the radial direction (x) measured by the LF-PIV and planar PIV is depicted in Fig. 24. Note that, both the planar PIV and LF-PIV data depicted in this figure are the averaged result in the axial range of $1.28 < y/D < 1.92$ (same with the height of the FOV of the LF-PIV). The result achieved by the dual-camera LF-PIV system is similar to the planar PIV. Whereas the single-camera

LF-PIV system cannot characterize the distribution tendency accurately. This further indicates that the measurement accuracy of the 3D velocity has been improved by the dual LF-PIV camera system.

6. Conclusion

This study proposes a dual-camera LF-PIV system along with the OS-SART for an accurate and faster 3D flow velocity measurement. The proposed system is first verified by the numerical reconstructions of particle fields and a Gaussian ring vortex field and further validated through the experimental measurements on a 3D circular jet flow. The concluding remarks achieved from this study are summarized as follows:

- The proposed system can reduce the particle reconstruction elongation effect significantly and improves the reconstruction spatial resolution by more than 10 times.
- The reconstruction efficiency of the OS-SART is at least twice of the conventional SART at the particle conventional of 0.1 ppm to 1 ppm, while the required memory space is only 1/12 of the latter.
- The synthetic 3D Gaussian ring vortex field and circular jet flow field can be measured accurately by the proposed system, whereas notable errors and poor accuracy are achieved by the single-camera LF-PIV system. Therefore, the capability of the proposed system for accurate flow velocity measurement is verified.

In future, the state-of-the-art shake-the-box(STB) Lagrangian particle tracking technique [37] will be considered to integrate with LF-PIV for improving the spatial resolution of 3D flow measurement.

Author Declaration

Conflict of interest

The authors declare that they have no known competing financial interests or personal relationships that could have appeared to influence the work reported in this paper.

Acknowledgements

The authors wish to express their gratitude to the National Natural Science Foundation of China (No. 51976038) for supporting this research.

References

[1] Kajitani L, Dabiri D. A full three-dimensional characterization of defocusing digital particle image velocimetry[J]. Measurement Science and Technology, 2005, 16: 790-804.

[2] Pereira F, Gharib M, Dabiri D, et al. Defocusing digital particle image velocimetry: A 3-component 3-dimensional DPIV measurement technique. Application to bubbly flows[J]. Experiments in Fluids, 2000, 29: S078-S084.

[3] Morton C, Yarusevych S, Scarano F. A tomographic particle image velocimetry investigation of the flow development over dual step cylinders[J]. Physics of Fluids, 2016, 28: 025104.

[4] He C, Wang P, Liu Y, et al. Flow enhancement of tomographic particle image velocimetry measurements using sequential data assimilation[J]. Physics of Fluids, 2022, 34: 035101.

[5] Mendelson L, Techet A H. Quantitative wake analysis of a freely swimming fish using 3D synthetic aperture PIV[J]. Experiments in Fluids, 2015, 56: 135.

[6] Belden J, Truscott T T, Axiak M C, et al. Three-dimensional synthetic aperture particle image velocimetry[J]. Measurement Science and Technology, 2010, 21: 125403.

[7] Schröder A, Schanz D. 3D Lagrangian particle tracking in fluid mechanics[J]. Annual Review of Fluid Mechanics, 2023, 55: 511-540.

[8] Novara M, Schanz D, Geisler R, et al. Multi-exposed recordings for 3D Lagrangian particle tracking with Multi-Pulse Shake-The-Box [J]. Experiment in Fluids, 2019, 60: 1-19.

[9] Scarano F. Tomographic PIV: Principles and practice[J]. Measurement Science and Technology, 2013, 24: 012001.

[10] Ihrke I, Restrepo J, Mignard-Debise L. Principles of light field imaging: Briefly revisiting 25 years of research[J]. IEEE Signal Processing Magazine, 2016, 33: 59-69.

[11] Ng R. Digital light field photography[D]. Stanford Univerisity, 2006: 1-203.

[12] Zhu X, Xu C, Hossain M M, et al. Approach to select optimal cross-correlation parameters for light field particle image velocimetry[J]. Physics of Fluids 2022, 34, 073601.

[13] Shi S, Ding J, Atkinson C, et al. A detailed comparison of single-camera light-field PIV and tomographic PIV[J]. Experiments in Fluids, 2018, 59: 1-13.

[14] Skupsch C, Brücker C. Multiple-plane particle image velocimetry using a light-field camera[J]. Opt Express 2013, 21: 1726.

[15] Mei D, Ding J, Shi S, et al. High resolution volumetric dual-camera light-field PIV[J]. Experiments in Fluids, 2019, 60: 132.

[16] Shi S, Ding J, New TH, et al. Light-field camera-based 3D volumetric particle image velocimetry with dense ray tracing reconstruction technique[J]. Experiments in Fluids, 2017, 58: 78.

[17] Song X, Gu M, Cao L, et al. A microparticle image velocimetry based on light field imaging[J]. IEEE Sensors Journal, 2019, 19: 9806-9817.

[18] Fahringer T W, Thurow B S. Filtered refocusing: A volumetric reconstruction algorithm for plenoptic-PIV[J]. Measurement Science and Technology, 2016, 27: 094005.

[19] Deem E A, Zhang Y, Cattafesta L N, et al. On the resolution of plenoptic PIV[J]. Measurement Science and Technology, 2016, 27: 084003.

[20] Zhu X, Zhang B, Li J, et al. Volumetric resolution of light field imaging and its effect on the reconstruction of light field PIV[J]. Optics Communications, 2020, 462: 125263.

[21] Andersen A. Simultaneous algebraic reconstruction technique (SART): A superior implementation of the ART algorithm[J]. Ultrasonic Imaging, 1984, 6: 81-94.

[22] Herman G T, Lent A. Iterative reconstruction algorithms[J]. Computers in Biology and Medicine, 1976, 6: 273-294.

[23] Zhu X, Wu Z, Li J, et al. A pre-recognition SART algorithm for the volumetric reconstruction of the light field PIV[J]. Optics and Lasers in Engineering, 2021, 143: 106625.

[24] Fahringer T W, Thurow B S. Plenoptic particle image velocimetry with multiple plenoptic cameras[J]. Measurement Science and Technology, 2018, 29: 075202.

[25] Zeng X, He C, Liu Y. GPU-accelerated MART and concurrent cross-correlation for tomographic PIV[J]. Experiments in Fluids, 2022, 63: 1-18.

[26] Zhu X, Hossain M M, Li J, et al. Weight coefficient calculation through equivalent ray tracing method for light field particle image velocimetry[J]. Measurement, 2022, 193: 110982.

[27] Fahringer T W, Lynch K P, Thurow B S. Volumetric particle image velocimetry with a single plenoptic camera[J]. Measurement Science and Technology, 2015, 26: 115201.

[28] Hall E M, Fahringer T W, Guildenbecher D R, et al. Volumetric calibration of a plenoptic camera[J].

Applied Optics, 2018, 57: 914.

[29] Shi S, Ding J, New TH, et al. Volumetric calibration enhancements for single-camera light-field PIV[J]. Experiments in Fluids, 2019, 60: 21.

[30] Thomas L, Tremblais B, David L. Optimization of the volume reconstruction for classical Tomo-PIV algorithms (MART, BIMART and SMART): Synthetic and experimental studies[J]. Measurement Science and Technology, 2014, 25, 035303.

[31] Xu F, Xu W, Jones M, et al. On the efficiency of iterative ordered subset reconstruction algorithms for acceleration on GPUs[J]. Computer Methods and Programs in Biomedicine, 2010, 98: 261-270.

[32] Hall E M, Guildenbecher D R, Thurow B S. Development and uncertainty characterization of 3D particle location from perspective shifted plenoptic images[J]. Opt Express, 2019, 27: 7997-8010.

[33] Cao L, Zhang B, Hossain M M, et al. Tomographic reconstruction of light field PIV based on a backward ray-tracing technique[J]. Measurement Science and Technology, 2021, 32: 044007.

[34] Guo C, Liu W, Hua X, et al. Fourier light-field microscopy[J]. Opt Express, 2019, 27: 25573.

[35] Gu M, Li J, Xu C. A modified Richardson–Lucy deconvolution for rapid reconstruction of light field μPIV[J]. Experiments in Fluids, 2022, 63: 1-15.

[36] Elsinga G E, Scarano F, Wieneke B, et al. Tomographic particle image velocimetry[J]. Experiments in Fluids, 2006, 41: 933-947.

[37] Schanz D, Gesemann S, Schröder A. Shake-The-Box: Lagrangian particle tracking at high particle image densities[J]. Experiments in Fluids, 2016, 57: 1-27.